Plane-wave-based electron tunneling through Au nanojunctions: Numerical calculations

A. Garcia-Lekue
Donostia International Physics Center (DIPC), Paseo Manuel de Lardizabal 4, E-20018 San Sebastian, Spain

L. W. Wang*
Computational Research Division, Lawrence Berkeley National Laboratory, Berkeley, California 94720, USA
(Received 4 March 2010; revised manuscript received 13 April 2010; published 9 July 2010)

Electron tunneling across a nanojunction is an important topic relevant to scanning tunnel microscope imaging, nanoconductance measurements, and nanoelectronic devices. To understand such tunneling phenomena, one needs to comprehend the electron-state coupling between the metal electrode and the vacuum, the dependence of such coupling on the shape of the electrode tip, and the dependence of the tunneling currents on the electrode-electrode distance. Due to the experimental difficulty to determine the exact atomic structure of the electrode tip, theoretical simulation can play an important role on such studies. This requires high-fidelity quantum-transport calculations for the tunneling system. However, most of the current quantum-transport calculations are performed using atom-centered localized basis sets, which cannot adequately describe the wave function in the vacuum region. In this work, we present tunneling-conductance calculations obtained using the transport calculation method introduced by Wang [Phys. Rev. B **72**, 045417 (2005)] and Garcia-Lekue and Wang [Phys. Rev. B **74**, 245404 (2006)]. Since this method employs a plane-wave basis set, it provides variational description for the electron wave functions in all real space. We will present results for the tunneling-current dependence on the electrode-electrode distance, the electrode wave functions in the vacuum region depending on the electrode shape, and electron state couplings between the vacuum and the electrode.

DOI: 10.1103/PhysRevB.82.035410 PACS number(s): 71.15.−m, 73.63.−b, 73.22.−f

I. INTRODUCTION

In recent years, different experimental techniques[1–4] have enabled the formation of current conducting atomic-size junctions, which are of great interest in view of their ultimate application to future nanoscale-device technologies. Depending on the distance between the electrodes of the junction, the conductance can vary several orders of magnitude when the applied bias voltage is low. Accordingly, two different regimes are usually distinguished: contact or high-conductance and tunneling or low-conductance regime.[5] The low-conductance or tunneling regime of such atomic-scale junctions has been thoroughly studied with the scanning tunneling microscope (STM).[6] In particular, an experimental quantity that can be extracted from STM experiments which may shed some light on the mechanism of electron tunneling is the apparent barrier height.[7,8] This quantity is obtained by measuring the variation in the tunneling current (I) as a function of the distance between both sides of the junction, i.e., between the tip and the apex (Δz). Although many experimental results of apparent barrier heights have been reported,[9–12] the effect of the detailed atomic structure of the junction on the apparent barrier height has not been extensively studied, due to the difficulty of experimentally investigating the tip atomic structure. Another interesting question is the coupling between the electronic states in the electrode and the electronic states and modes in the vacuum, as well as the way the atomic structure of the electrode tip affects such coupling. The amplitude of the tunneling is mainly dependent on the evanescent electron states in the vacuum region. These evanescent states have different symmetries and, therefore, can decay very differently. It is, thus, interesting to understand the coupling between the electrode states and the electron wave functions in the vacuum. Such knowledge and experimentally measured tunneling current can perhaps provide information about the atomic structure of the electrode tips.

Given the high sensitivity of conductance to atomic-structure details, it is necessary to perform *ab initio* simulations using first-principles methods such as those based on density-functional theory (DFT). In particular, the more widely employed method combines the nonequilibrium Green's function formalism (NEGF) and DFT electronic structure obtained with a localized atomic basis.[13–20] In principle, DFT methods cannot rigorously handle nanojunctions, open systems that are infinite, nonperiodic and out of equilibrium because DFT describes systems in their ground state. Besides, for almost any practical DFT calculation, one needs to consider some reasonable approximation for the *xc* functional. Therefore, DFT is just one of the best choices currently available for quantum-transport calculations and the so-called NEGF-DFT approach should be treated as a practical method rather than a rigorously exact theory.

With regard to the basis set used within the NEGF-DFT transport calculations, there are issues of the variational completeness of the atomic basis sets especially when dealing with tunneling problems. Sometimes it is necessary to introduce ghost orbitals, where their locations and orbital types are not unique.[21] For example, the tunneling current crossing a vacuum gap cannot be described adequately by the conventional atomic basis set due to the lack of flexibility to describe the tunneling wave functions in the vacuum region. Similarly, in a STM image simulation the use of atomic basis sets often leads to shorter tip to substrate distances than in

the experiments, again due to the lack of flexibility to describe the wave function. The most widely used basis set in material science simulation is the plane-wave-basis set. This basis set is considered to be variationally more complete than the localized basis, especially when pseudopotentials are used. Thus, numerically more accurate results can be expected from plane-wave calculations. There are recent approaches which generate the localized Wannier functions as the localized basis starting from the plane-wave-basis set for NEGF-DFT calculation. But approximation needs to be made to truncate the number of Wannier functions and the interactions between Wannier functions.[22] Another alternative route within plane-wave-based DFT is given by the novel quantum-kinetic approach introduced in Ref. 23. In this approach, a time-dependent Hamiltonian is used to describe an external circular electric field within a periodic boundary condition and a quantum-mechanical Liouville master equation is solved including the electron-phonon interaction.

Recently, we have developed a procedure to efficiently calculate the scattering states in quantum-transport problems using a plane-wave-basis set.[24–26] Our approach is valid for any applied bias voltage since the current is calculated self-consistently, and can include exact evanescent states, which are also calculated using plane waves. The scattering states are solved exactly in a fast and numerically stable procedure with a computational time similar to a conventional ground-state calculation. Based on these scattering states one can straightforwardly calculate the transmission coefficients and the corresponding electronic current. Since the plane-wave-basis set is variational enough to describe the wave function in the vacuum region, this quantum-transport-calculation method is expected to be well suited to describe the tunneling problem.

Using this plane-wave-based transport approach, we have investigated the influence of the detailed atomic structure on the apparent barrier height of Au nanojunctions and we show that this approach is indeed very appropriate for the description of transport properties in the tunneling regime. The rest of the paper is organized as follows. In Sec. II we explain the plane-wave-based quantum-transport-calculation method. In Sec. III, illustrative results for some Au nanojunction model systems are provided. Finally, in Sec. IV, we state our conclusions.

II. NUMERICAL METHOD

A. Elastic quantum-transport calculation

The current that flows through the model Au nanojunction shown in Fig. 1 can be calculated using the Landauer formula

$$I = \frac{2e}{h}\int_{\mu_L}^{\mu_R}\sum_n T_n(E)dE, \tag{1}$$

where μ_L and μ_R are the left (L) and right (R) electrode Fermi energies, assuming that the current flows from right to left, and $T_n(E)$ is the transmission coefficient for the nth right-hand electrode band with energy E.

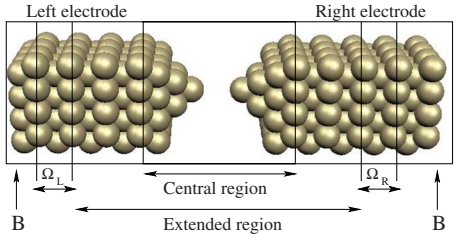

FIG. 1. (Color online) Model Au nanojunction, where $\Omega_{L(R)}$ represents the L(R) primary unit cell.

The transmission coefficient can be calculated using different methods, such as the most commonly employed non-equilibrium Green's function method. An alternative way to obtain $T_n(E)$ involves the calculation of the scattering states of the system, which are the solution of the following Schrödinger equation:

$$H\psi_{sc}(r) = E\psi_{sc}(r), \tag{2}$$

where $H=[-\frac{1}{2}\nabla^2+V(r)]$ is the single-particle Hamiltonian and $V(r)$ includes the nonlocal potential V_{nonloc}. The scattering states $\psi_{sc}(r)$ must fulfill the boundary conditions of the problem given by

$$\psi_{sc}(r) = \begin{cases} \phi_m^{R*}(r) + \sum_{n\neq m} B_n^R \phi_n^R(r) & \text{if } z\to\infty, \\ \sum_n A_n^L \phi_n^{L*}(r) & \text{if } z\to-\infty, \end{cases} \tag{3}$$

where z is chosen as the direction of current propagation. $\phi_n^{L(R)}(r)=u_{n,k_n}(r)\exp(ik_n^{R(L)}z)$ $[\phi_n^{L(R)*}(r)]$ represents the left-going (right going) waves in the L and R electrodes, respectively, and $\phi_m^{R*}(r)$ is an incoming running wave from the right electrode with energy E. $E_n^{R(L)}(k_n^{R(L)})=E$ are the electrode band structures, and the summation Σ_n in Eq. (3) stands for all band n and $k_n^R(L)$ which satisfy $E_n^{R(L)}(k_n^{R(L)})=E$. Hence, Eq. (3) describes an incoming running wave $\phi_m^{R*}(r)$ from the right electrode m, which is scattered back through outgoing running waves $B_n^R\phi_n^R(r)$ at the right electrode and transmitted into left-going running waves $A_n^L\phi_n^{L*}(r)$ at the left electrode. The transmission coefficient for channel m resulting from this scattering event can be calculated as

$$T_m(E) = \frac{\left(\sum_n |A_n^L|^2 [dE_n^L(k)/dk]|_{k=k_n^L}\right)}{[dE_m^R(k)/dk]|_{k=k_m^R}}. \tag{4}$$

Hence, the main ingredient in our transport approach is the scattering state ψ_{sc}. In the following, the method employed in this work to obtain ψ_{sc} is briefly described.

B. Scattering-state calculation

In order to solve Eq. (2), we impose auxiliary periodic boundary conditions at the boundaries B of the system so that our open boundary problem is transformed into a conventional closed boundary problem.[24] Under these conditions we can solve the following linear equation:

$$(H-E)\psi_l(r) = W_l(r), \tag{5}$$

where $W_l(r)$ represent some perturbation functions that are nonzero only near the boundaries B of the system. Equation (5) is solved using the conjugate gradient method and the solutions $\psi_l(r)$ will be denoted as system states.

Far enough from the molecular region the system potential will decay to the potential of the electrode. Consequently, at L and R electrode primary cells Ω_L and Ω_R (Fig. 1), each system state ψ_l with energy E can be decomposed using the running and evanescent electrode states at the same energy E. In order to properly account for the evanescent states, the complex band structure of the electrode can be calculated following the procedure introduced in Ref. 25. Alternatively, approximated evanescent states can be employed in the system state decomposition, as described in Ref. 24. This approximation might be useful for speedy calculations. However, one should in this case pay special attention to the possible appearance of ill-behaved evanescent states. Therefore, the use of exact or evanescent electrode states will depend on the system under investigation.

In the extended region shown in Fig. 1, which consists of the molecule and the short electrodes, one can linearly combine the system states to generate the scattering states of Eq. (2) as follows:

$$\psi_{sc} = \sum_{l=1}^{M} C_l \psi_l(r), \tag{6}$$

where the coefficients $\{C_l\}$ are chosen so that the boundary condition of Eq. (3) is satisfied at Ω_L and Ω_R. Introducing the electrode-states based decomposition of the system states at $\Omega_{L(R)}$ in the linear combination of Eq. (6) and taking into account the boundary conditions of Eq. (3), leads to a small dimension linear equation for $\{C_l\}$, which can be solved easily. Details on these equations and how to solve them are described in Refs. 24 and 25. From the solution of these equations one can then construct the scattering states using Eq. (6). Such scattering states are correct only in the extended region of Fig. 1 since near the boundary B they do not satisfy Eq. (2) due to the existence of W_l perturbation functions. However, outside the region beyond Ω_L and Ω_R, we can obtain the scattering states by propagating the nonzero electrode states at $\Omega_{L(R)}$ into $z \to \pm\infty$. In this way, we can construct the scattering state over the whole space.

This method is general and can be applied to any Hamiltonian. In this work we use a plane-wave Hamiltonian both for the system states as well as for the complex band-structure calculation. As a result, we are able to calculate scattering states for an open-boundary problem using plane waves. From the knowledge of the scattering states, we can straightforwardly calculate the transmission coefficients and the current using Eqs. (1) and (4).

C. Apparent barrier height

According to a one-dimensional (1D) description of the tunneling barrier,[27,28] the tunneling current I at small bias voltage V is proportional to $V\exp(-1.025\Delta z\sqrt{\Phi})$, where Δz is the tip-apex separation in Å and Φ is given in electron volt. Hence, for constant bias, the apparent barrier height can be expressed as the rate of change in the logarithm of the current with the tip-apex distance,[8] as follows:

$$\Phi = 0.952\left(\frac{d\ln I}{d\Delta z}\right)^2 \tag{7}$$

with Φ in electron volt, Δz in Å, and arbitrary units for I.

In the low-bias regime only the states at the Fermi level take part so according to Eq. (1) the current is proportional to the total transmission coefficient at the Fermi level given by

$$T(E_F) = \sum_m T_m(E_F), \tag{8}$$

where the summation Σ_m stands for all band m that cross the real band structure of the electrode at the Fermi level. It then follows from Eq. (7) that the apparent barrier height in the low-bias limit can be extracted from the slope of the logarithm of $T(E_F)$ with the electrode separation or vacuum-gap width.

Therefore, the calculation of the apparent barrier height is performed by first calculating the scattering states at the Fermi level for different electrode separations in the tunneling regime. From the scattering states the transmission coefficients for different channels and electrode separations are obtained, and finally the apparent barrier height is extracted following Eq. (7).

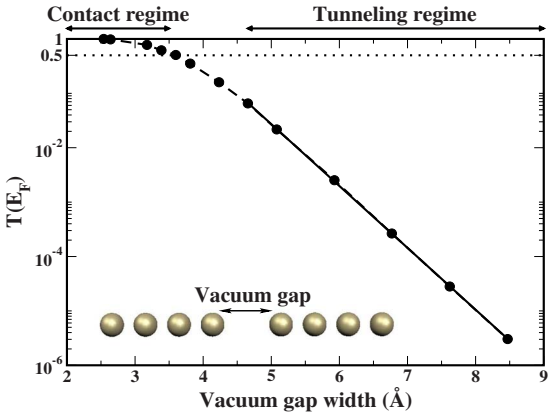

FIG. 2. (Color online) Total transmission at the Fermi level as a function of the vacuum-gap width.

III. RESULTS AND DISCUSSION

A. Linear Au chain with plane waves

In order to verify that our plane-wave-based method reproduces very accurately not only the contact but also the tunneling regime, and hence yields an accurate result for the apparent barrier height, we first investigate the simple model Au nanojunction shown in the inset of Fig. 2. This junction consists of an initially long linear atomic Au chain which is broken in the central region.

The current flowing through this junction has been obtained based on the transport approach described in Sec. II, in combination with a standard plane-wave program.[29] Calculations are performed using norm conserving pseudopoten-

tials and local-density approximation (LDA) for the exchange-correlation function. Some eigenenergy errors are expected from LDA calculations but our Fermi energy result agrees reasonably well with the experiment. In order to properly describe evanescent states in the gap, we have used a cylindrical 60 Ryd plane-wave cutoff. This means that the plane-wave vectors will lie inside a cylinder which has no cutoff in the z direction.[25] For the electrode and for the ground-state central region, the calculations are converged with respect to the number of k points. For the transport calculation, only Γ point in the x,y directions is included. In terms of total current, this might not be fully converged but we do not expect any changes in terms of the slope of the current as a function of distance. Besides, this will not affect our scattering state wave-function analysis where only a few states are selected. A zero applied bias voltage has been considered and the charge density is calculated self-consistently from ground-state calculations.

For the calculation of the scattering states, the use of approximated evanescent states has been found to yield very good results for the decomposition of the system states at L(R) boundaries. Consequently, all the calculations presented in this work have been obtained using approximated evanescent states for the Au electrodes.

As shown in Fig. 2, we have calculated $T(E_F)$ for the broken linear Au chain using different electrode separations ranging from contact to tunneling regime. In contact regime, the total transmission at Fermi level is ~ 1, which is the well-known result for a linear atomic Au chain with a single transmission channel. As the two sides of the junction are moved apart, the transmission decays smoothly. For large enough vacuum gaps, we enter the tunneling regime and the transmission exhibits a perfect exponential decay. From the exponential tail of the transmission curve we get an apparent barrier height of ~ 6.2 eV.

Before moving onto more thorough investigations of the effect of geometry on the apparent barrier height, we first compare our plane-wave transport calculation results with the atomic-orbital basis set results. For this purpose, we have done the same calculation as in Fig. 2 but using a NEGF-DFT transport approach with atomic orbitals.[14,30,31] An isolated chain was used for both localized atomic orbital and plane-wave-based calculations so both approaches include Γ point only and the comparison is fair. As seen in Fig. 3, plane waves (solid lines) and atomic orbitals (dashed lines) give the same result in contact regime. However, as the vacuum gap increases the results start to deviate, and well into the tunneling regime, the atomic orbitals are not able to nicely reproduce the exponential decay of the transmission. This problem can be overcome by introducing ghost atoms, i.e., floating orbitals that do not have electrons nor pseudopotential associated. Making use of ghost atoms, the transmission obtained with atomic orbitals (dashed-dotted line) can be made to have exponential decay and it agrees with the plane-wave calculation result. However, we found that the results depend strongly on the location and number of ghost atoms and are difficult to converge. This might raise the issue of reliability of that approach in tunneling regime.

On the other hand, in the case of systems involving a large number of atoms, transport calculations using plane waves can be significantly more expensive than those based on localized atomic orbitals. As a consequence, the choice of using a plane-wave or a localized atomic basis set will depend on the system under investigation and on the size of the vacuum region between the electrodes.

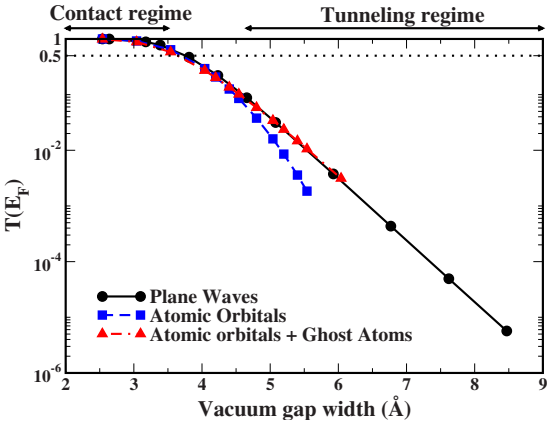

FIG. 3. (Color online) Total transmission at the Fermi level as a function of the vacuum-gap width obtained using plane waves (solid line), atomic orbitals (dashed line), and atomic orbitals with ghost atoms (dashed-dotted line).

B. Au nanojunctions: Geometric effects

In the following, we will focus on more realistic geometries, as those shown in Fig. 4. System 1 consists of two facing 4×4-Au(001) surfaces, periodic in the (x,y) plane

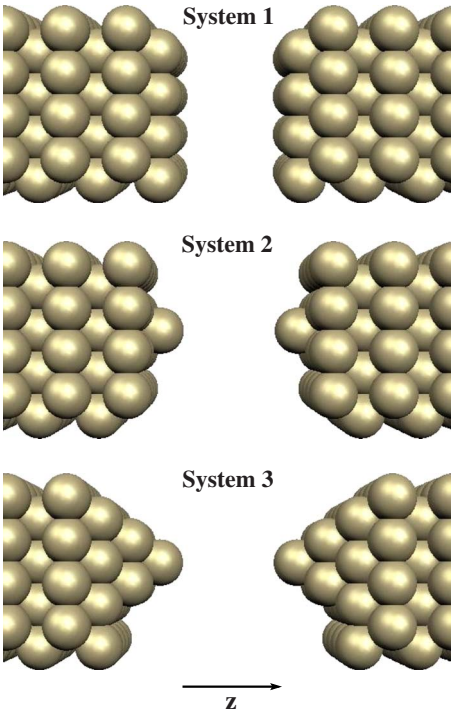

FIG. 4. (Color online) System 1 (top panel): 4×4-Au(001) flat surfaces. System 2 (middle panel): 4×4-Au(001) with an adatom on each surface. System 3 (bottom panel): 4×4-Au(001) with a five-atom pyramid on each surface.

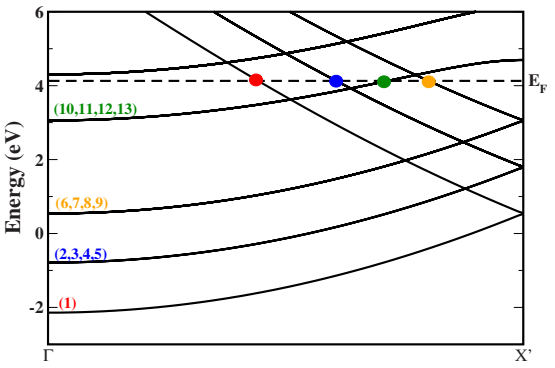

FIG. 5. (Color online) Real band structure of the 4 $\times$4-Au(001) electrode.

perpendicular to the direction of propagation (z). By placing a single Au adatom or a five-atom pyramidal bases on each 4×4-Au(001) surface we construct system 2 or system 3, respectively.

At zero bias, only states at the Fermi surface are involved in the tunneling transport, which involve only s states. As a result, we have removed the d electrons of Au from our pseudopotential method to reduce the cost of calculation. We have checked that this approximation is appropriate by calculating the transmission at Fermi level for a linear Au chain using pseudopotentials with and without d bands. In both cases, we get the same results for $T(E_F)$ (not shown here). Accordingly, the zero-bias transport calculations for systems 1, 2, and 3 can be performed using s-only pseudopotentials, which makes the investigation of those systems computationally more accessible. Note that, if the Au electrode is attached to a molecule, it might be necessary to include d states in the calculation, in order to get the band alignment correctly between the molecule and the Au electrode.

The real band structure for the 4×4-Au(001) electrode obtained with the s-only pseudopotential is shown in Fig. 5, where k_z represents the wave vector in the direction of propagation (z). With respect to $K_\parallel$, the wave vector in the direction perpendicular to the current propagation, we consider the Γ-point only approximation. This means that only $K_\parallel=0$ is included in the calculations. As discussed before, although this might not converge the total current, we do not expect it to affect the slope in Fig. 3.

Using the Γ-point only approximation we find that four bands cross the Fermi level, as represented by circles in Fig. 5. While the $n=1$ band is nondegenerated, the other three bands are four times degenerated. Hence, and according to Eq. (8), the total transmission at Fermi level will be the sum of the contributions from four different channels originated by 13 different incoming electrode states. The degeneracy of the bands can be understood in terms of the K_{xy} of the fcc unit cell, which are all folded into the $K_\parallel=0$ of the electrode supercell. Using the reciprocal lattice vectors, K_{xy} can be expressed as $K_{xy}=\frac{2\pi}{4a}(n_x,n_y)$ where n_x and n_y are integer numbers and represent the components of the wave vector in the x and y directions, respectively, and $a=4.18$ Å is the Au lattice constant. The nondegenerated band would correspond to the $(n_x,n_y)=(0,0)$ case, and the {2,3,4,5}, {6,7,8,9}, and {10,11,12,13} bands would correspond to (n_x,n_y) equal to $(\pm1,0),(0,\pm1)$; $(\pm1,\pm1)$; and $(\pm2,0),(0,\pm2)$ cases, respectively.

Based on the procedure described in Sec. II, and using an s-like Au pseudopotential both for the electrode and for the central region, we have proceeded with the transport calculations. The transmission coefficients at the Fermi level for systems 1, 2, and 3 have been calculated as a function of the vacuum-gap width. Besides, in order to extract information about the properties of each of the tunneling states involved, we have calculated the contribution of each channel separately. Figure 6 shows each of these contributions together with the total transmission for system 1 (upper panel), system 2 (middle panel), and system 3 (lower panel). For the three systems, all transmission channels exhibit perfect exponential decay in tunneling regime. Fitting the transmission curves to the 1D model, we extract the apparent barrier height for each channel. In the case of flat surfaces (system 1), the four channels exhibit different barriers whereas for corrugated surfaces (systems 2 and 3) all channels have the same barrier height. As will be discussed below, this is because in the corrugated cases, the electrode states couple to different vacuum states compare to the flat-surface case.

We now analyze the cause of different apparent barrier heights for different electrode states and different electrode shapes. At the vacuum region, as deduced from the single-electron Schrodinger equation, the barrier height in the tunneling direction (z direction) is determined by the potential height and the (x,y) direction kinetic energies in the middle plane between the two electrodes. In order to study the potential in the middle plane, we have plotted the x,y planar averaged potential of systems 1, 2, and 3 as a function of z in Fig. 7. This corresponds to the case when the vacuum-gap width d is 10 Å. We see that, the potential height V relative to the bulk Fermi energy E_F in the middle plane is about 5.8 eV, and it is the same for all the three systems. We have also calculated the potential for a strictly isolated flat surface, i.e., with no other flat surface in front of it. In this case, we get a potential W (work function) of 6.1 eV, larger than the potential height V. However, V should equal W when the vacuum-gap width tends to infinity. Therefore, from the fact that V and W are different, we can conclude that even at 10 Å, the potential height is not converged. However, since our apparent barrier heights are obtained from the slope of $\log[T(d)]$ at around 10 Å, we will use this value of V in our following analysis. Note that our LDA calculated work function of 6.1 eV is larger than the experimental value of 5.4 eV.[32] This difference is caused by the LDA eigenenergy errors.

We next calculate the (x,y) direction kinetic energies of the scattering states in the midplane (z_m) as follows:

$$K=\frac{\int[|\partial\psi_{sc}(x,y,z_m)/\partial x|^2+|\partial\psi_{sc}(x,y,z_m)/\partial y|^2]dxdy}{2\int|\psi_{sc}(x,y,z_m)|^2dxdy}, \tag{9}$$

where ψ_{sc} represents the scattering state at the Fermi level. If we consider the incoming electrode states independently, then we get ψ_{sc} and the corresponding kinetic energy for

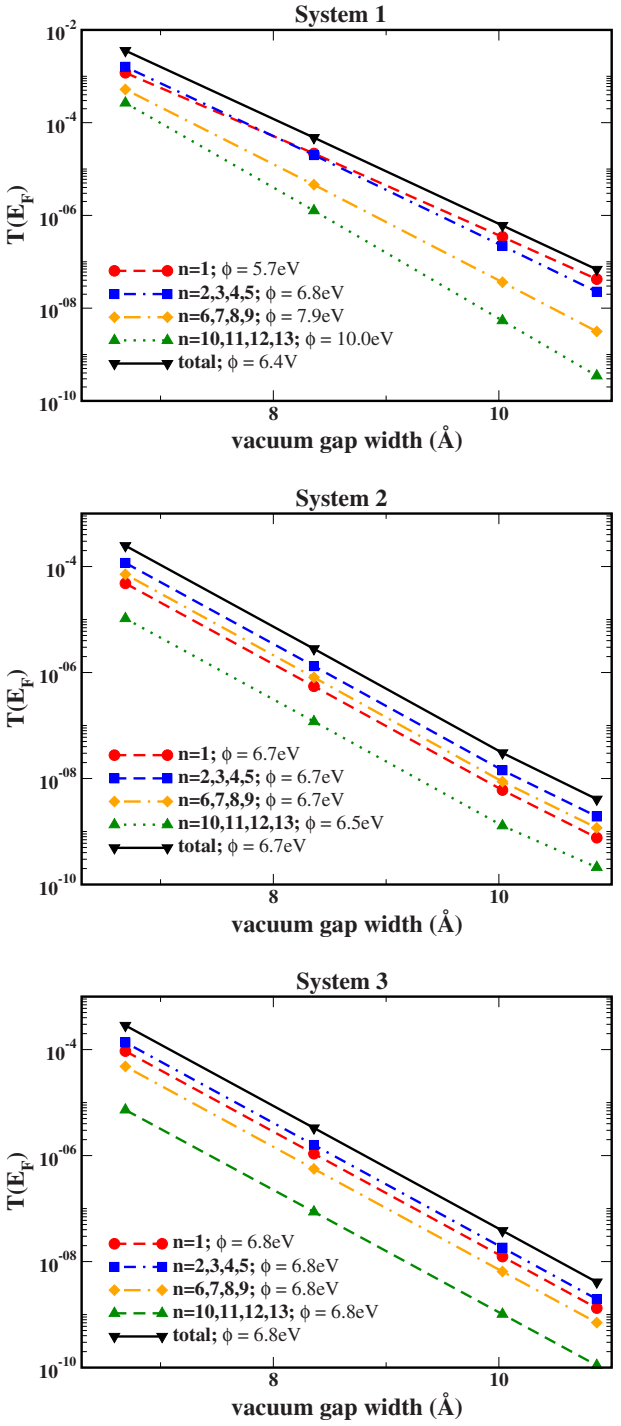

FIG. 6. (Color online) Transmission for each electrode channel and total transmission at Fermi level as a function of vacuum-gap width. Upper, middle, and lower panels correspond to system 1, 2, and 3, respectively.

each transmission channel. The sum of the kinetic energy and the potential height of the system should give the barrier height of that specific channel. This is confirmed in Table I where the kinetic energy (K), the sum of the kinetic energy and the potential ($K+V$), and the apparent barrier height (Φ) obtained by fitting the transmission curve are shown. The close agreement between the $K+W$ and Φ is a bit surprising

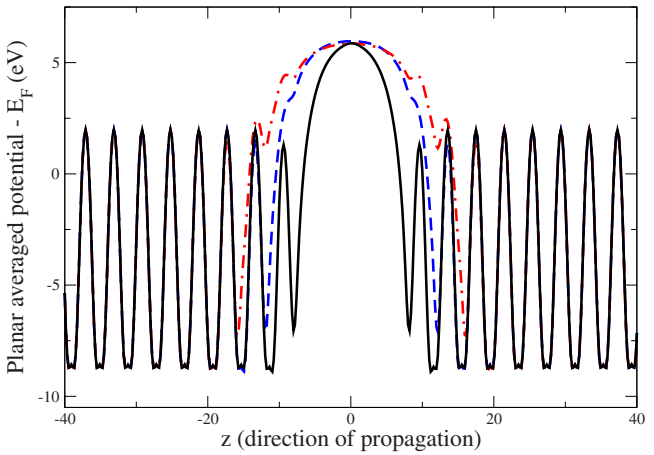

FIG. 7. (Color online) (x,y) planar averaged potential of system 1 (solid line), system 2 (dashed line), and system 3 (dashed-dotted line). The origin of z direction is placed in the midplane between electrodes.

since, as can be seen from Fig. 7 the barrier potential is not a flat plateau.

A nice way to visualize the scattering states and the coupling of the electrode states to vacuum states is presented in Fig. 8, where $\ln|\psi_{sc}(x,y,z)|^2$ for the $(n_x,n_y)=(0,0)$ scattering state is plotted. One interesting feature is that in the flat surface, the (0,0) electrode state is coupled with a flat vacuum state (with a very small modification of its amplitude in the (x,y) plane following the 4×4 atomic arrangement of the electrode). As a result, the (x,y) kinetic energy in the midplane is almost zero, as reported in Table I. On the other hand, for the corrugated cases, the original flat front (0,0) electrode state is coupled with a concave wave front, spherical-like state. This is most predominant for system 3,

TABLE I. (x,y) kinetic energy (K), ($K+V$), and barrier height (ϕ). The barrier heights obtained from the fitted total transmission curve are 6.4 eV, 6.7 eV, and 6.8 eV for systems 1, 2, and 3, respectively.

State index	K (eV)	$K+V$ (eV)	ϕ (eV)
	System 1		
1	6.31×10^{-5}	5.80	5.72
2,3,4,5	1.07	6.87	6.80
6,7,8,9	2.15	7.95	7.87
10,11,12,13	4.3	10.10	10.00
	System 2		
1	0.83	6.63	6.71
2,3,4,5	0.95	6.75	6.68
6,7,8,9	0.96	6.76	6.69
10,11,12,13	1.02	6.82	6.50
	System 3		
1	0.95	6.75	6.79
2,3,4,5	0.93	6.73	6.77
6,7,8,9	0.93	6.73	6.75
10,11,12,13	0.86	6.66	6.71

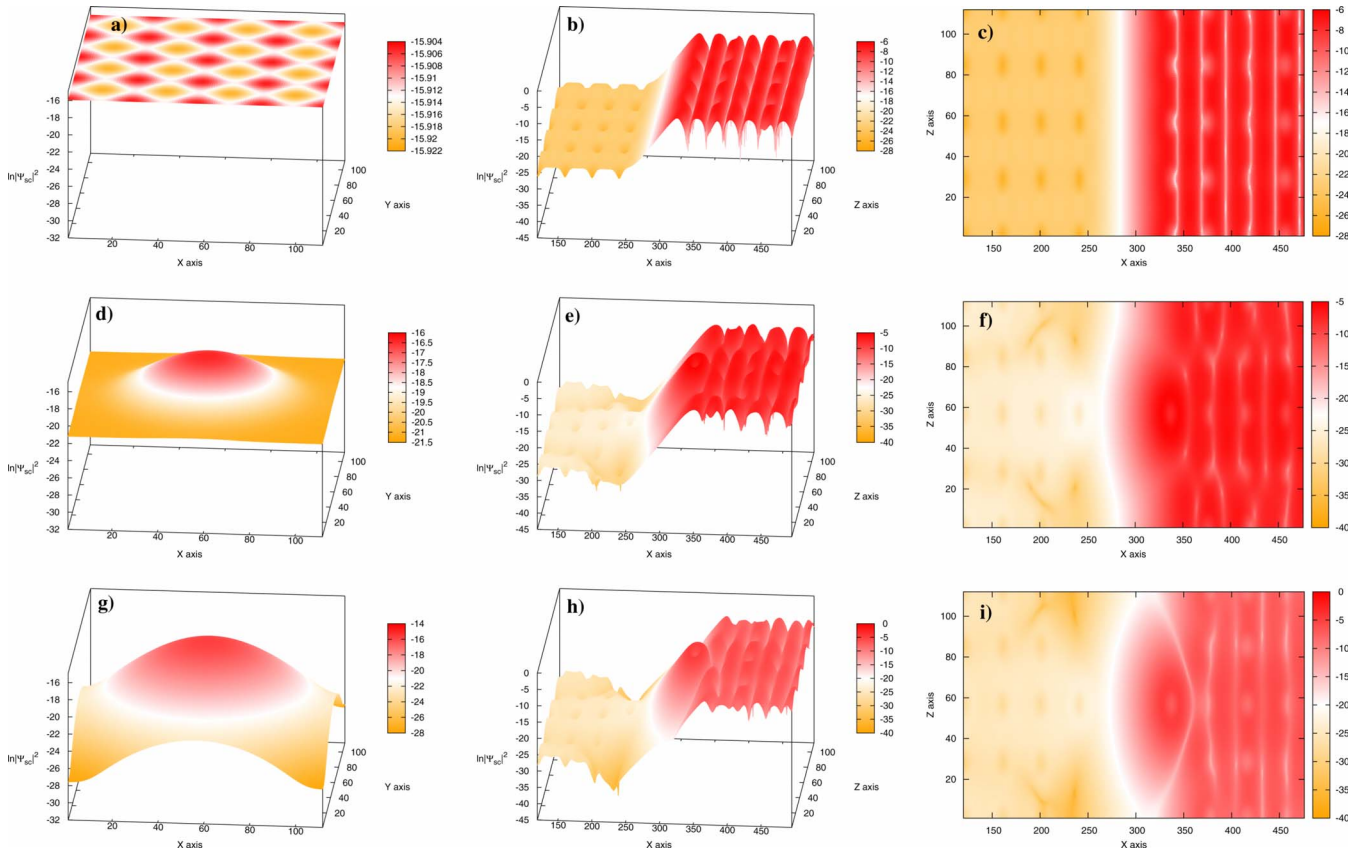

FIG. 8. (Color online) Representation of the $(n_x,n_y)=(0,0)$ scattering states of system 1 (upper panels), system 2 (middle panels), and system 3 (lower panels). (a), (d), and (g) panels: three-dimensional (3D) plots of $\ln|\psi_{sc}(x,y,z)|^2$ on the XY plane for Z in the middle of the gap. (b), (e), and (h), and (c), (f), and (i) panels: 3D and two-dimensional (2D) plots of $\ln|\psi_{sc}(x,y,z)|^2$ on the XZ plane for Y in the middle of the gap, respectively.

which has a pyramid shape. As shown in Table I, such a spherical vacuum wave function has a large (x,y) direction kinetic energy, which raises the apparent barrier height. It is thus interesting to note that each corrugated atom at the surface of the electrode can behave like an antenna which emits spherical electron waves.

Note that, other (n_x,n_y) states for the flat electrode (system 1) will only couple to the corresponding (n_x,n_y) vacuum states (which can be confirmed from the scattering state plots, although not shown here). As a result, their midplane kinetic energy is: $\frac{1}{2}(\frac{2\pi}{4a})^2(n_x^2+n_y^2)$, as shown in Table I. This explains their different apparent barrier height. An interesting question is why all electrode states have approximately the same apparent barrier height (Table I), although their current amplitudes are different, as shown in Fig. 6. This will be explained in the following section.

C. Odd/even states for corrugated Au nanojunctions

As we concluded from the results of the transmission coefficients shown in Fig. 6, all channels exhibit the same decaying behavior in systems 2 and 3. This is due to the fact that all incoming electrode states couple to the vacuum-free states. However, this might depend on our choice of incoming electrode states. Right now, they are the distinct K_{xy} states as described by

$$\phi_{\mathbf{k}}^m = \sum_{\mathbf{G}} U_{\mathbf{G}}^m(\mathbf{k}) e^{i(\mathbf{G}-\mathbf{k})\cdot\mathbf{r}} \tag{10}$$

$\mathbf{G}$ being the reciprocal lattice vectors of the system. The Bloch vector $\mathbf{k}$ is given by $\mathbf{k}=(\mathbf{K_{xy}},k_z)$, where in terms of reciprocal lattice vectors $\mathbf{K_{xy}}=\frac{2\pi}{4a}(n_x,n_y)$. As a result, these electrode states do not have an odd/even symmetry, and they will all couple to the spherical vacuum state.

A more interesting choice of the incoming electrode state is the odd/even states. The electrode states given by Eq. (10) can be combined in order to obtain electrode states with sine $[\sin(\frac{2\pi}{4a}n_y y)]$ or cosine $[\cos(\frac{2\pi}{4a}n_y y)]$ odd/even character. Due to their symmetry, not all the newly built electrode states will couple to the spherical vacuum state. Cosinelike (even) electrode states will couple to the vacuum free electron state but sinelike (odd) electrode states will not. Consequently, sinelike electrode states will decay much faster into the vacuum and the corresponding transmission coefficients will then be much smaller.

For example, let us apply this procedure to the bands {2,3,4,5}. The corresponding electrode states, constructed following Eq. (10) do not have odd/even symmetry and as previously mentioned, they all show the same decaying behavior (see middle and bottom panels of Fig. 6). We now combine these four electrode states in order to obtain two

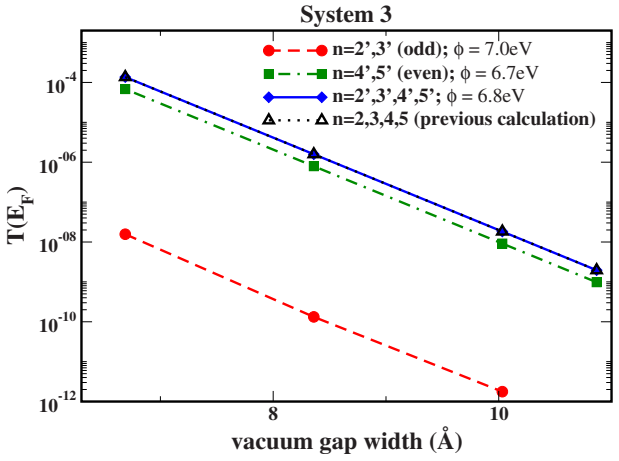

FIG. 9. (Color online) Transmission for odd/even electrode channels of bands {2,3,4,5} and total transmission (for those bands) at Fermi level as a function of vacuum-gap width.

odd ($\{2',3'\}$) and two even ($\{4',5'\}$) electrode states. The transmission coefficients for ($\{2',3'\}$) and ($\{4',5'\}$) are shown in Fig. 9. As predicted, the transmission coefficients of the odd states (dashed line) are much smaller than those of the even states (dashed-dotted line), which indicates that most of the electron propagation is carried out by even states. Therefore, odd states decay more rapidly than even states and exhibit a larger apparent barrier height. This is confirmed by fitting the transmission curves in Fig. 9: the apparent barrier height of odd ($\{2',3'\}$) and even ($\{4',5'\}$) electrode states is 7.0 eV and 6.7 eV, respectively. We have also verified that the sum of the transmission for even and odd electrode states, i.e., the sum of the transmission from $\{2',3',4',5'\}$ electrode states (solid line of Fig. 9) gives exactly the same as the sum of the contributions from the {2,3,4,5} spherical electrode states (dotted line of Fig. 9).

Finally, we have represented the scattering states corresponding to odd and even electrode states. The upper and lower panels of Fig. 10 show the scattering states for an odd ($\{2'\}$ or $\{3'\}$) and an even ($\{4'\}$ or $\{5'\}$) electrode state of system 3, respectively. We observe that the scattering state corresponding to the odd electrode state exhibits a node on the XY plane in the middle of the gap [Fig. 10(a)]. This indicates that the odd electrode state does not couple to the vacuum spherical state and that consequently, its decaying length in the direction of propagation (z) is extremely short, as shown in Figs. 10(b) and 10(c). For the even state on the other hand, the scattering state on the (x,y) plane has spherical symmetry [Fig. 10(d)], which is an indication of its strong coupling to the vacuum spherical state. As a result, this state decays further from the surface in the z direction, as shown in Figs. 10(e) and 10(f). From the decaying behavior of these scattering states, one can conclude that the corresponding transmission coefficients will be much larger and that the barrier height will be lower for the even electrode state. This agrees with the results shown in Fig. 9 and shows that even states are the most relevant channels for electron propagation in the tunneling regime.

IV. CONCLUSION

In this work, electron tunneling through Au nanojunctions has been thoroughly investigated by means of a plane-wave-based quantum transport calculation method. Special emphasis has been placed on the study of the apparent barrier height, an experimentally measurable quantity strongly influenced by electron-tunneling mechanisms. We present theoretical results for the tunneling-current dependence on the electrode separation, which exhibits perfectly exponential decay. By fitting the current versus electrode-separation curves we are able to extract theoretical values of the apparent barrier height.

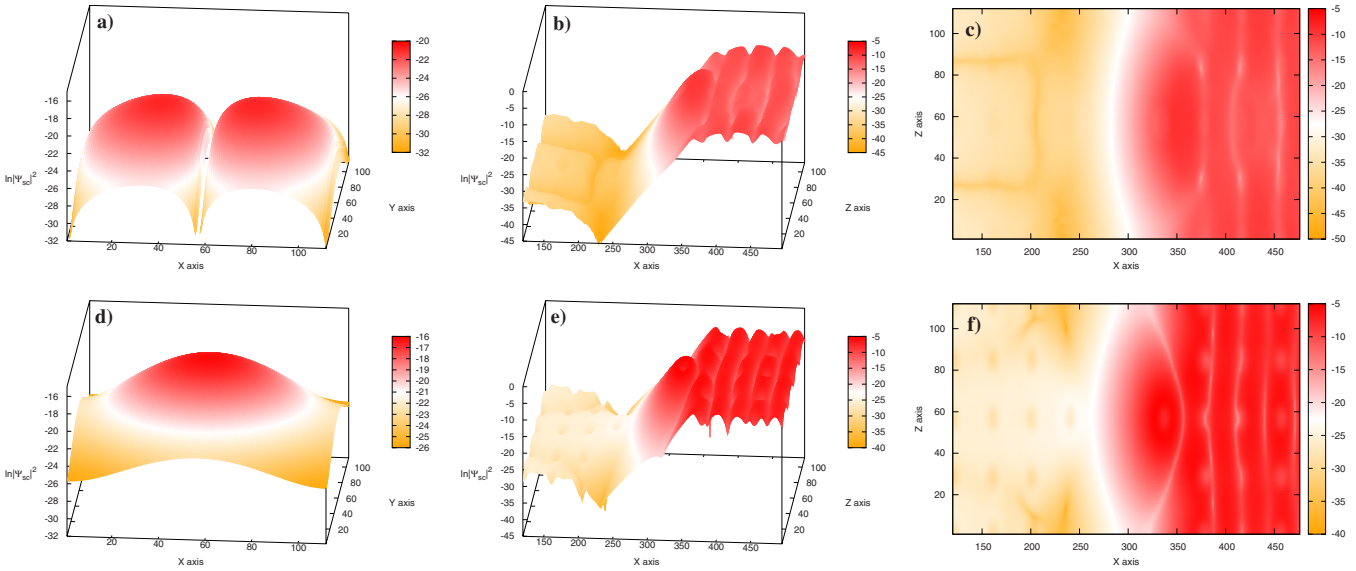

FIG. 10. (Color online) Representation of scattering states of system 3 corresponding to odd ($\{\hat{2},\hat{3}\}$) (top) and even ($\{\hat{4},\hat{5}\}$) (bottom) electrode states. (a) and (d) panels: 3D plots of $\ln|\psi_{sc}(x,y,z)|^2$ on the XY plane for Z in the middle of the gap. (b) and (e) and (c) and (f) panels: 3D and 2D plots of $\ln|\psi_{sc}(x,y,z)|^2$ on the XZ plane for Y in the middle of the gap, respectively.

We have investigated how the detailed atomic structure of the junction and the coupling between the electrode and the vacuum states affects the apparent barrier height. We find that in corrugated surfaces the electrode states couple to different vacuum states compared to the flat surface case. Accordingly, for flat surfaces different channels exhibit different barriers whereas for corrugated surfaces all channels have the same barrier. In order to gain understanding about these effects, we have derived an analytical formula for the apparent barrier height in the midplane between the electrodes, which is given by the sum of the potential height and the kinetic energy in the plane perpendicular to the tunneling direction. The values of the barrier calculated using this formula agree very well with the values obtained from fitting the tunneling current curves.

Further knowledge on the tunneling mechanisms has been extracted from the visualization of the scattering states. We show that for the flat surface the original flat electrode state is coupled with a flat vacuum state while for the corrugated nanojunctions it is coupled with a spherical-like, concave wave front. As a result, each corrugated atom of the electrode can behave like an antenna which emits spherical electron waves.

In conclusion, we have shown that our plane-wave-based transport method provides a very accurate description of the scattering wave functions in the vacuum region, and it is therefore highly appropriate for the investigation of transport properties in the tunneling regime. Our results encourage us to pursue further studies of electron-tunneling problems employing plane waves.

ACKNOWLEDGMENTS

We thank A. Arnau and N. Lorente for stimulating discussions, and T. Frederiksen for his help with transiesta calculations. Support from the Basque Departamento de Educación, UPV/EHU (Grant No. IT-366-07), the Spanish Ministerio de Ciencia e Innovación (Grant No. FIS2007-6671-C02-00), the ETORTEK program funded by the Basque Departamento de Industria and the Diputacion Foral de Guipuzcoa, and the DMS/BES/SC of the U.S. Department of Energy under Contract No. DE-AC02-05CH11231 are gratefully acknowledged. It used the resources of the National Energy Research Scientific Computing Center (NERSC).

*Corresponding author; wmbgalea@lg.ehu.es

[1] D. M. Eigler, C. P. Lutz, and W. R. Rudge, Nature (London) **352**, 600 (1991).
[2] C. Joachim, J. K. Gimzewski, R. R. Schlittler, and C. Chavy, Phys. Rev. Lett. **74**, 2102 (1995).
[3] J. M. Krans, C. J. Muller, I. K. Yanson, T. C. M. Govaert, R. Hesper, and J. M. van Ruitenbeek, Phys. Rev. B **48**, 14721 (1993).
[4] M. A. Reed, C. Zhou, C. J. Muller, T. P. Burgin, and J. M. Tour, Science **278**, 252 (1997).
[5] T. Frederiksen, N. Lorente, M. Paulsson, and M. Brandbyge, Phys. Rev. B **75**, 235441 (2007).
[6] A. Aviram, C. Joachim, and M. Pomerantz, Chem. Phys. Lett. **146**, 490 (1988).
[7] G. Binnig, H. Rohrer, C. Gerber, and E. Weibel, Appl. Phys. Lett. **40**, 178 (1982).
[8] N. D. Lang, Phys. Rev. B **37**, 10395 (1988).
[9] Y. Hasegawa, J. F. Jia, K. Inoue, A. Sakai, and T. Sakurai, Surf. Sci. **386**, 328 (1997).
[10] K. Miya, A. Sinsarp, M. Sasaki, and S. Yamamoto, Jpn. J. Appl. Phys., Part 2 **44**, L31 (2005).
[11] M. Saida, K. Horikawa, T. Sato, S. Yamamoto, and M. Sasaki, Surf. Sci. **600**, L139 (2006).
[12] J. Kröger, H. Jensen, and R. Berndt, New J. Phys. **9**, 153 (2007).
[13] J. Taylor, H. Guo, and J. Wang, Phys. Rev. B **63**, 245407 (2001).
[14] M. Brandbyge, J.-L. Mozos, P. Ordejón, J. Taylor, and K. Stokbro, Phys. Rev. B **65**, 165401 (2002).
[15] K. Stokbro, J. Taylor, M. Brandbyge, J.-L. Mozos, and P. Ordejón, Comput. Mater. Sci. **27**, 151 (2003).
[16] S.-H. Ke, H. U. Baranger, and W. Yang, J. Chem. Phys. **122**, 074704 (2005).
[17] Ž. Crljen, A. Grigoriev, G. Wendin, and K. Stokbro, Phys. Rev. B **71**, 165316 (2005).
[18] A. Grigoriev, J. Sköldberg, G. Wendin, and Ž. Crljen, Phys. Rev. B **74**, 045401 (2006).
[19] S. H. J. Zhang, R. Li, Z. Qian, R. Han, Z. Shen, X. Zhao, and Z. Xue, Nanotechnology **16**, 3057 (2005).
[20] A. R. Rocha, V. M. García-Suárez, S. Bailey, C. Lambert, J. Ferrer, and S. Sanvito, Phys. Rev. B **73**, 085414 (2006).
[21] S. García-Gil, A. García, N. Lorente, and P. Ordejón, Phys. Rev. B **79**, 075441 (2009).
[22] A. Calzolari, N. Marzari, I. Souza, and M. Buongiorno Nardelli, Phys. Rev. B **69**, 035108 (2004).
[23] R. Gebauer and R. Car, Phys. Rev. B **70**, 125324 (2004).
[24] L. W. Wang, Phys. Rev. B **72**, 045417 (2005).
[25] A. Garcia-Lekue and L. W. Wang, Phys. Rev. B **74**, 245404 (2006).
[26] A. Garcia-Lekue and L. W. Wang, Comput. Mater. Sci. **45**, 1016 (2009).
[27] J. G. Simmons, J. Appl. Phys. **34**, 1793 (1963).
[28] J. K. Gimzewski and R. Möller, Phys. Rev. B **36**, 1284 (1987).
[29] http://hpcrd.lbl.gov/linwang/PEtot/PEtot.html
[30] The SIESTA (Ref. 31) and TranSIESTA (Ref. 14) packages were used for the NEG-DFT calculations. The corresponding SIESTA calculations employ a split-valence double-zeta plus polarization basis for Au atoms, the generalized gradient approximation for the exchange-correlation function, a cutoff of 200 Ry for the real-space grid integrations, and the Γ point approximation for the sampling of the three-dimensional Brillouin zone.
[31] J. Soler, E. Artacho, J. Gale, A. Garcia, J. Junquera, P. Ordejon, and D. Sanchez-Portal, J. Phys. Condens. Matter **14**, 2745 (2002).
[32] *CRC Handbook of Chemistry and Physics*, 87th ed., edited by David R. Lide (CRC Press, Boca Raton, FL, 2007).